A Particle MHD Simulation Approach with Application to a Global Comet-Solar Wind Interaction Model

Richard D. Sydora
Department of Physics and
Institute of Geophysics and Planetary Physics
University of California at Los Angeles
Los Angeles, California 90024 USA

Joachim Raeder
Institut für Geophysik, Universität zu Köln
Albertus Magnus Platz, D5000 Köln 41, W. Germany

ABSTRACT

The formulation and properties of a Lagrangian magnetofluid represented by a distribution of finite-sized particles is described. A numerical simulation algorithm is outlined in detail for time-advancing the particle quantities of the fluid (position, momentum and temperature) as well as their accumulation on a mesh in order to compute the magnetic and pressure forces. Microscopic processes are introduced into the MHD model such as the Hall current and viscosity effects. The Alfvèn and magnetosonic waves are shown to obey the correct dispersion for nearly all wavenumbers within the fundamental Brillouin zone of the mesh and a model shock tube simulation shows the model adequately handles shocks and discontinuities. The particle MHD model is used to investigate the global solar wind-cometary plasma interaction. The results reveal the develpment of a distinct bow shock, propagation of upstream and downstream MHD waves and cometary ion accumulation in the shock region. Finally, a closed set of multi-fluid equations, within the framework of the particle MHD model, is derived as well as numerical methods for archieving larger time steps.

1. Introduction

In the fluid description of a plasma it is assumed that the plasma can be broken into a collection of fluid elements which are smaller than the characteristic

length over which plasma quantities change significantly. The particles which make up the fluid element can be held together by fields or by collisions with neighboring particles. By coarse-graining of time scales and the introduction of magnetohydrodynamic (MHD) forces rather than the Lorentz force, it is possible to use equations with fewer degrees of freedom to understand the dynamics of the fluid elements. An essential approximation is that all particles in the fluid element remain in near thermal equilibrium locally. This allows the definition of a center of mass velocity and a temperature derived from local isotropic particle distributions.

There is no single approach in the solution of the MHD equations because of the diversity of the physical phenomena. Each class of problems requires special numerical methods in the detailed investigation of the linear and nonlinear evolution of the system. In the general case, which we consider here, where the fluid and magnetic energy strongly interact, explicit conservative methods are applicable for solving the MHD equations. In the ideal case, the Eulerian form of the MHD equations produces advection, sound waves and Alfvèn waves. It is the advection phenomenon which is the main source of difficulty in numerical simulation of the MHD equations [1]. Therefore, it is desireable to work in the moving frame of the fluid and treat the equations of motion of the fluid elements in a Lagrangian manner.

In the analagous way of using particle simulation to solve the many body problem of a continuous phase fluid, described by the Vlasov equation, a particle approach to solving the MHD equations can be formulated. It has been shown [2] that robust numerical schemes for solving the full set of compressible MHD equations using techniques of conventional particle simulation models, for accurate

description of macroscopic plasma behavior is possible. The 'graininess' of the procedure overemphasizes short wavelength plasma behavior, however, methods for minimizing the effects at these scales have been developed. In fact, this has been the central focus of attention for accurate simulation of kinetic plasma behavior using particle methods over the last twenty years so many techniques are available [3].

In section 2 an extensive discussion of the numerical methods used in solving the MHD equations with the particle MHD approach is presented. It is also shown that this procedure is amenable to the addition of microscopic processes which can affect the macroscopic plasma behavior. These include the effects of Hall currents and viscosity. If the fluid is viscous, momentum and energy are diffused through the fluid by microscopic particle motion. A careful study of this process is made to prevent diffusive entropy production from numerical noise and to understand its effects on MHD fluctuations.

This is important for the applications presented in sections 3 and 4, namely the formation of discontinuities and shock waves in a magnetofluid as well as the physical processes which occur when two fluids interpenetrate each other. This situation is encountered when ionizing neutral gas from a comet interacts with the high speed solar wind plasma flow. In section 4 two physical processes are considered in some detail. First, the ion mass flow and distribution surrounding a comet as well as the effects of cometary ion mass loading of the solar wind. Second, the development of MHD fluctuations and their propagation upstream and downstream of the cometary bow shock.

In section 5 a discussion of the extensions of the model to include multiple fluids and the Lagrangian form of the equations to describe the coupling of the

fluids is presented. Also, an outline of numerical procedures for using larger time steps employing implicit forms of the equations is given. This is particularly useful for problems where the Alfvèn wave frequency is high and the numerical methods become quite restrictive. Finally, section 6 contains a brief summary and conclusions.

2. The Particle MHD Approach

A particle method of solving equations on the level of magnetohydrodynamics has been introduced [2] and extensively developed [4]. Fluid elements are treated as particles and the orbits of these fluid elements are integrated using the MHD forces acting on them. Any short range forces between particles are minimized due to the finite size of these fluid elements, which essentially means that they may overlap. The particles are carriers of local fluid information, such as density, momentum and temperature and move through a fixed background grid. The grid holds average fluid quantities, the force fields and the magnetic field. A procedure must be established to assign quantities from the particles onto the grid and vice versa in an accurate and efficient manner. This topic is an essential part of the algorithm and will be discussed later.

In the conventional ideal MHD approach all fluid properties are transported or advected by the motion of the fluid [5,6,7,8]. If we separate the advective motion from the local changes, the MHD equations take a much simpler, namely a Lagrangian form. Most numerical algorithms suffer from problems in treating the advective part of the equations and a great deal of work has been invested to develop monotonous numerical schemes to solve these mixed hyperbolic/elliptic equations of compressible hydro- and magnetohydrodynamics [9]. By treating the fluid in a Lagrangian manner these problems are intrinsically avoided. Spu-

rious solutions, like negative densities are impossible. There is also no need to introduce artificial diffusivities, but a new problem, namely the multistreaming of particles may appear. We will discuss this topic later in this section after we have outlined the basic equations and the numerical algorithm.

2.1 Basic Equations

A fluid element k is characterized by its position $\vec{x}_k$, its velocity $\vec{v}_k$ and its temperature T_k. The changes of the particle position, velocity and temperature are given by a pressure field p, a magnetic field $\vec{B}$ and the bulk density, velocity and temperature fields n, $\vec{v}$ and T. The Langrangian form of the magnetohydrodynamic equations is then written as follows [10]:

$$\frac{d\vec{x}_k}{dt} = \vec{v}_k \tag{1}$$

$$\frac{d\vec{v}_k}{dt} = \frac{1}{n \cdot m_k} \cdot \left\{ -\vec{\nabla}p - \frac{1}{4\pi}\vec{B} \times \left(\vec{\nabla} \times \vec{B}\right) \right\} \tag{2}$$

$$\frac{dT_k}{dt} = \frac{1}{n} \cdot \left\{ -(\gamma - 1)p\vec{\nabla}\vec{v} + \left(\frac{c}{4\pi}\right)^2 \cdot ((\vec{\nabla} \times \vec{B}) \cdot \eta \cdot (\vec{\nabla} \times \vec{B})) + \vec{\nabla}\left(\kappa \cdot \vec{\nabla}T\right) \right\} \tag{3}$$

where we have introduced the material properties of the fluid: γ: ratio of specific heats, η: tensor of electical conductivity and κ: tensor of thermal conductivity as well as the particle mass m_k. An equation of state relates the pressure to the temperature and density. Here we assume that the fluid behaves like an ideal gas:

$$p = n \cdot T \tag{4}$$

Equation (4) also states that we measure the temperature in energy units. These equations are closed by an induction equation for the magnetic field, which may be written in Eulerian form since the magnetic field is a grid quantity:

$$\frac{\partial \vec{B}}{\partial t} = \vec{\nabla} \times \left(\vec{v} \times \vec{B}\right) - \frac{c^2}{4\pi}\vec{\nabla} \times \{\eta \cdot (\vec{\nabla} \times \vec{B})\} \tag{5}$$

At this point we may incorporate a great deal more physical effects into the particle MHD model in a straightforward manner [11]. Let us take into account that electrons and ions can slip relative to one another across the magnetic field. This effect occurs at the microscale of the plasma, but has an influence on the macroscopic fluid behavior by introducing a Hall current. Since the timescale we are interested in is given by the Alfvèn speed, we may assume, that the electrons instantaneously adjust their velocity to the ion motion, i. e. we may treat the electrons as a massless fluid. The electron momentum equation then reads:

$$(\vec{E} + \frac{1}{c}\vec{v} \times \vec{B}) + \frac{1}{n|e|}\vec{\nabla}p_e = 0 \tag{6}$$

By virtue of (6) we may derive a modified induction equation which becomes:

$$\frac{\partial \vec{B}}{\partial t} = c\vec{\nabla} \times \left\{ \frac{1}{c}\vec{v} \times \vec{B} - \frac{c}{4\pi}\eta \cdot \left(\vec{\nabla} \times \vec{B}\right) + \frac{1}{4\pi n|e|}\vec{B} \times \left(\vec{\nabla} \times \vec{B}\right) \right\} \tag{7}$$

Here we assumed that the electron pressure is negligible, otherwise equation (7) would contain a term proportional to $\vec{\nabla}p_e$ and the ion momentum equation (2) would be altered. Equation (7) says that neglecting collisions, the magnetic field moves with the electron fluid but because of the ion inertia they are allowed to slip across the field. The Hall current term fits nicely into our equations without any need to compute the current explicitly.

Before we start to outline the numerical algorithm, we wish to put the equations into a dimensionless form. We accomplish this by introducing a scale for every quantity and writing: $t = t_0 t'$, $\vec{B} = B_0 \vec{B}'$, etc., where the primed variables are dimensionless and the suffix '$_0$' indicates the scaling variable. Equations (1-4) and (7) then read, if we neglect all diffusive effects ($\eta = 0$, $\kappa = 0$) and drop the primes:

$$\frac{d\vec{x}_k}{dt} = \vec{v}_k \tag{8a}$$

$$\frac{d\vec{v}_k}{dt} = \frac{1}{nm_k}\left\{ -\frac{T_0}{v_0^2}\vec{\nabla}p - \frac{v_A^2}{v_0^2}\vec{B}\times\left(\vec{\nabla}\times\vec{B}\right)\right\} \tag{8b}$$

$$\frac{dT_k}{dt} = -(\gamma-1)T\vec{\nabla}\vec{v} \tag{8c}$$

$$p = n\cdot T \tag{8d}$$

$$\frac{\partial\vec{B}}{\partial t} = \vec{\nabla}\times\left(\vec{v}\times\vec{B}\right) + \alpha\vec{\nabla}\times\left\{\frac{1}{n}\vec{B}\times\left(\vec{\nabla}\times\vec{B}\right)\right\} \tag{8e}$$

Here we introduced the Alfvèn speed $v_A = B_0/(4\pi m_i n_0)^{\frac{1}{2}}$, the Hall parameter $\alpha = v_A^2/(\omega_{ci}v_0 r_0)$ and the ion gyrofrequency $\omega_{ci} = |e|B_0/(cm_i)$. Equation (8b) simplifies further if we set the velocity normalization equal to the temperature normalization: $v_0^2 = T_0$:

$$\frac{d\vec{v}_k}{dt} = \frac{1}{nm_k}\left\{ -\vec{\nabla}p - \frac{2}{\beta}\vec{B}\times\left(\vec{\nabla}\times\vec{B}\right)\right\} \tag{8b'}$$

where β is the ratio of the plasma pressure to the magnetic pressure: $\beta = 2T_0/v_A^2 = 8\pi p_0/B_0^2$. For numeric convenience we choose $r_0 = \Delta = 1$, where Δ is the gridsize. We may then interpret the Hall parameter α in the following manner:

$$\alpha\cdot\beta = \frac{v_{th}}{r_0\omega_{ci}} = \frac{\rho_L}{\Delta}$$

assuming the mean thermal speed v_{th} equals the sound speed within a factor of the order of unity. The Hall parameter is thus the ratio of the ion Larmor radius ρ_L to the gridsize with a factor of the plama β. The Hall parameter times the plasma β should therefore be less than unity to be consistent with the assumption that the plasma behaves like a fluid. A larger value of $\alpha\cdot\beta$ means that finite Larmor radius effects may have to be taken into account.

2.2 The Numerical Algorithm

2.2.1 Time Discretisation We wish to develop a second order accurate time stepping scheme for the system of equations (8). To advance the velocity and

the position in time we may use a leapfrog scheme as is commonly employed in particle codes. The magnetic field equation (8e) may be solved using a two step Lax-Wendroff method [1,9]. A time–centered scheme is possible except for the temperature equation (8c). This may be seen best if we write the equations in the following general form:

$$\frac{d\vec{x}_k}{dt} = \vec{v}_k \tag{9a}$$

$$\frac{d\vec{v}_k}{dt} = \vec{F}_v(n,T,\vec{B}) \tag{9b}$$

$$\frac{dT_k}{dt} = F_T(n,T,\vec{v}) \tag{9c}$$

$$\frac{\partial\vec{B}}{\partial t} = F_B(n,\vec{v},\vec{B}) \tag{9d}$$

There is no intrinsic time–centering for this system of equations because a quantity on the left hand side should also appear on the right hand side staggered by a half timestep. However, an integration scheme, which is virtually time centered and second order accurate in time, can be written as follows:

$$\vec{v}_k^{\,n+1/2} - \vec{v}_k^{\,n-1/2} = \Delta t\vec{F}_v(n^n, T^{*n}, \vec{B}^n) \tag{10a}$$

$$\vec{x}_k^{\,n+1} - \vec{x}_k^{\,n} = \Delta t\vec{v}_k^{\,n+1/2} \tag{10b}$$

$$T_k^{n+1/2} - T_k^{n-1/2} = \Delta t F_T(n^n, \vec{v}^n, T^{*n}, \vec{B}^n) \tag{10c}$$

where the integers and half integers represent the time level and we made use of a temperature predictor:

$$T^{*n} = \frac{3}{2}T^{n-1/2} - \frac{1}{2}T^{n-3/2}$$

The magnetic field may then be pushed using the two step Lax-Wendroff scheme. The predictor step is:

$$\vec{B}^{n+1/2} =< \vec{B}^n > + \frac{\Delta t}{2}\vec{F}_B(n^n, \vec{v}^n, \vec{B}^n) \tag{11}$$

where $< ... >$ denotes a spatial average over nearest neighboring mesh values. To obtain the velocity at time level n we have to split (10a) into two subcycles. After we pushed the velocity a second half timestep to level $n + 1/2$ and collect the fluid velocity onto a grid we may push the magnetic field through the full timestep:

$$\vec{B}^{n+1} = \vec{B}^{n} + \Delta t \vec{F}_B(n^{n+1/2}, \vec{v}^{n+1/2}, \vec{B}^{n+1/2}) \tag{12}$$

It can be shown [2] that this time discretisation scheme conserves both energy and momentum and is second order accurate.

2.2.2 Spatial Discretisation The treatment of the spatial derivatives is in principle straightforward. Experience shows however, that the particle MHD scheme tends to emphasize short wavelengths and thus a finer treatment of the spatial derivatives is desirable. Therefore, a staggered, double mesh for the computation of the pressure and magnetic forces is used [4,12]. This procedure reduces particle random motion arising from the sound wave portion of the spectrum. All fluid variables and the magnetic field at timestep n are defined on the integral position mesh, while the pressure force term and intermediate values of $\vec{B}$ are on the half position mesh. In evaluating spatial derivatives, the full position mesh is transferred to the half position mesh with the following procedure:

$$(\frac{\partial A}{\partial x})_{i+1/2,j+1/2} = (A_{i+1,j} - A_{i,j} + A_{i+1,j+1} - A_{i,j+1})/2\Delta x \tag{13}$$

In addition to this type of differencing, densities and velocities have to be accumulated on the half position mesh in order to compute the force term in a properly centered manner.

2.2.3 Particle Interpolation It has been pointed out earlier that an interpolation scheme has to be established in order to assign particle quantities to

gridpoints and vice versa. Most known methods have been used, namely Fourier transform methods with dipole and quadrupole interpolation, area weighting (cloud in cell) and nearest gridpoint weighting. The simplest method, the nearest gridpoint weighting, gives very poor results with respect to particle random motion (noise) and dispersion properties. The other two methods are comparable, but the area weighting has two distinct advantages. First, there is less dispersion for both Alfvèn and sound waves at large k-modes. Even though both schemes have second order accuracy, the waves disperse more at higher k-modes for the subtracted dipole scheme. Second, complicated boundary conditions or nonregular meshes may be intractable with the dipole scheme, whereas they are straightforwardly implemented with the area weighting. A comparative study on these weighting schemes has been done by Brunel et al. [4]. We will define the area weighting scheme, as it is implemented in our code in the form of the discrete operators:

P: grid $\rightarrow$ particles

G: particles $\rightarrow$ grid

The operators P and G are just the discrete form of particle weighting functions and allow for a more convenient notation of the algorithm, where the particular form of the weighting scheme does not appear any more (see [3] for a discussion of weighting schemes). In the following we define these operators for the area weighting and for a linear weighting scheme. The gridspacing is taken to be unity and 'a' refers to the particle size. We restrict ourself to the one dimensional case while the extension to higher dimensions is straightforward. The offset, x_0, is 1. for the integral grid and 0.5 for the staggered grid.

First, we define for a particle k, its grid index, i_k and weighting factors:

a) area weighting:

$$i_k = INT(x_k + x_0 + 0.5)$$

$$dx_k = x_k + x_0 - i_k$$

$$w_{-1,k} = max\{(a-1)/2 - dx_k, 0\}/a$$

$$w_{0,k} = max\{(a+1)/2 - |dx_k|, 0\}/a$$

$$w_{1,k} = max\{(a-1)/2 + dx_k, 0\}/a$$

b) linear weighting

$$i_k = INT(x_k + x_0)$$

$$dx_k = x_k + x_0 - i_k$$

$$w_{-1,k} = 0$$

$$w_{0,k} = 1. - dx_k$$

$$w_{1,k} = dx_k$$

where the function INT truncates its argument to the next lower integer. The operators then have the following form:

$$p_k = P_k(g) = w_{-1,k} g_{i_k-1} + w_{0,k} g_{i_k} + w_{1,k} g_{i_k+1} \tag{16}$$

$$g = G(p) = \{g_i, i = 1, NG | g_i = \sum_{k=1}^{NP} p_k(\delta_{i,i_k-1} w_{-1,k} + \delta_{i,i_k} w_{0,k} + \delta_{i,i_k+1} w_{1,k})\} \tag{17}$$

where g is a grid quantity, p is a particle quantity, NP is the number of particles, NG is the number of grid points, and δ is the Dirac delta function.

Due to the fact that the linear scheme (b) needs much less computational operations and (a) does not improve results significantly we will use the scheme (b) throughout for our computations. Note also, that for a particle size a=1, the scheme (a) reduces to (b).

2.2.4 Multistreaming and Particle Drag Since the simulation model treats elements of the fluid like particles, fluid elements should not flow through each other. This multistreaming effect can be avoided by a relative drag term between particles in one cell [2]. This means that we introduce a new force term for the particles, but in such a way, that the net momentum change of all particles in one cell due to this extra force is zero. This procedure effectively minimizes the diffusive entropy production (noise, numerical heating of particles), keeping the velocity and internal energy a single valued function. Here we will outline two approaches to implement such a drag term.

First, we assume the drag term to be proportional to the difference of the particle velocity and the velocity of all particles in one cell (this velocity is computed anyhow). The following term must then be added to the right side of (8b):

$$-\nu_0 \cdot (\vec{v}_k - \vec{v}) \tag{18}$$

where ν_0 is the proportionality constant, $0 \leq \nu_0 \leq 1$, $\vec{v}_k$ is the particle velocity and $\vec{v}$ is the mean velocity at the position of the particle. This drag term corresponds to a Krook viscosity and it can be shown, that it conserves momentum. We will therefore refer to ν_0 as a viscosity.

A second approach is to make the constant ν_0 a function of other variables, like the velocity gradient. At each timestep the viscosity then becomes a function of the spatial coordinates: $\nu(\vec{x})$. Care must now be taken to implement this coordinate dependent viscosity in order to conserve momentum. A scheme with this property may be written as follows:

$$\vec{v}^* = \frac{G(\{\nu(\vec{x}_k) \cdot \vec{v}_k\})}{G(\{\nu(\vec{x}_k)\})} \tag{19}$$

and the drag term corresponding to (18) becomes:

$$-\nu(\vec{x}_k) \cdot (\vec{v}_k - P(\vec{v}^*)) \tag{20}$$

where the operators G and P are defined in equations (16) and (17). We will consider here a viscosity type given by Landshoff [13], where the viscosity is linear in the velocity gradient, and in the one dimensional case:

$$\nu(x) = \alpha\delta|\frac{\partial v}{\partial x}| = \nu_0|\frac{\partial v}{\partial x}| \tag{21}$$

where α is of the order of unity and δ corresponds to some typical shock thickness or large spatial gradient layer scale length. Tests with this viscosity type on a shock will be shown in section 3.

We should note here, that although the application of a viscous drag term is to overcome a weakness of the algorithm, particle multistreaming may be a true physical process, like a collisionless relative drift of two distinct fluids. In such a case the multistreaming may be limited by the growth of an instability and by MHD fluctuations. The particle MHD approach may then have superior properties in describing such phenomena as compared with other MHD models. We will return to this topic in section 5.

2.2.5 Outline of the Algorithm We will now give a compact form of the algorithm. For all variables the superscript refers to the time level and the subscript 's' at grid values refers to the half integer position, staggered mesh. The subscript 'k' indicates a quantity of particle k.

At time level n the following quantities are known:

$\vec{x}_k^n$, $\vec{v}_k^{n-1/2}$, ρ^n, ρ_s^n, n^n, $\vec{v}^{n-1/2}$, $T^{n-1/2}$, $T^{n-3/2}$, $\vec{B}^n$

a) predict temperature

$$T^n = \frac{3}{2}T^{n-1/2} - \frac{1}{2}T^{n-3/2}$$

b) compute forces for a half timestep

$$\vec{F}_{p,s} = -\frac{\Delta t}{2\rho_s^n}\vec{\nabla}(n^n \cdot T^n)$$

$$\vec{F}_B = -\frac{\Delta t}{\beta\rho^n}\vec{B}^n \times (\vec{\nabla} \times \vec{B}^n)$$

c) push velocity half timestep

$$\vec{v}_k^n = \vec{v}_k^{n-1/2} + P_k(\vec{F}_B) + P_k(\vec{F}_{p,s})$$

$$\vec{v}^n = G(\{n_k \cdot \vec{v}_k^n\})$$

d) push magnetic field first half timestep

$$\vec{B}^{n+1/2} = <\vec{B}^n> + \frac{\Delta t}{2}\vec{\nabla} \times \{\vec{v}^n \times \vec{B}^n + \frac{\alpha}{n^n}\vec{B}^n \times (\vec{\nabla} \times \vec{B}^n)\}$$

e) push velocities, position, temperature

$$\vec{v}_k^{n+1/2} = \vec{v}_k^n + P_k(\vec{F}_B) + P_k(\vec{F}_{p,s}) + \Delta t\nu_0(P_k(\vec{v}^n) - \vec{v}_k^n)$$

$$\vec{x}_k^{n+1/2} = \vec{x}_k^n + \frac{\Delta t}{2}\vec{v}_k^{n+1/2}$$

$$T_k^{n+1/2} = T_k^{n-1/2} - \Delta t(\gamma - 1)P_k(T^n\vec{\nabla} \cdot \vec{v}^n)$$

$$\vec{v}^{n+1/2} = \frac{G(\{n_k \cdot \vec{v}_k^{n+1/2}\})}{G(\{n_k\})}$$

$$T^{n+1/2} = \frac{G(\{n_k \cdot T_k^{n+1/2}\})}{G(\{n_k\})}$$

$$n^{n+1/2} = G(\{n_k\})$$

$$\vec{x}_k^{n+1} = \vec{x}_k^{n+1/2} + \frac{\Delta t}{2}\vec{v}_k^{n+1/2}$$

$$n^{n+1} = G(\{n_k\})$$

$$\rho^{n+1} = G(\{n_k m_k\})$$

$$\rho_s^{n+1} = G_s(\{n_k m_k\})$$

f) push magnetic field a full step

$$\vec{B}^{n+1} = \vec{B}^n + \Delta t \vec{\nabla} \times \{\vec{v}^{n+1/2} \times \vec{B}^{n+1/2} + \frac{\alpha}{n^{n+1/2}} \vec{B}^{n+1/2} \times (\vec{\nabla} \times \vec{B}^{n+1/2})\}$$

g) $n = n + 1$, return to a) for next timestep

In this algorithm we also assigned a density n_k and a mass m_k to each particle in order to be able to handle large density gradients and different particle species. The treatment of different particle species in this manner is not consistent with the moment equations for multiple fluids, since there is only one common pressure and temperature [10]. Nevertheless it may be applied here as long as the differential velocity between different species is small, as is the temperature difference between them. This is the same assumption made in other studies, where a multispecies plasma is treated as a single fluid, although this fact is not always explicitly stated [14,15]. By introducing a drag term we make the same assumption, but we loose information about drifts between the different constituents of the plasma. We will outline a self-consistent multispecies algorithm in section 5.

Note that there are two passes through the particles every timestep in c) and in e). Inclusion of a spatial dependent viscosity requires an extra pass between d) and e) in order to collect the quantity $\vec{v}^*$. Of course proper boundary conditions have to be taken into account in the finite difference and particle-grid operators. Their implementation is straightforward for the interpolation scheme used and will not be outlined here (see [3,16]).

2.2.6 Restrictions of the Algorithm In order to investigate the numerical stability of the particle MHD algorithm we consider the magnetic induction equation (8e). We perform a signal analysis on the induction equation by assuming the perturbations are of the form $B^n_{jk} = T^n W_{jk}$, where $T^n \sim e^{-in\omega\Delta t}$,

$W_{jk} \sim e^{ikx_j}$ and $x_j = j\Delta$ is a grid index and n refers to the time level. Using a linearized form of the equation we determine whether the amplitude for the time dependent factor, T_k, grows, decays or remains constant in time. If T^n grows in amplitude then all signals, including the errors, will be amplified and the scheme is unstable. Computing the ratio, $|T^{n+1}|/|T^n| \equiv g$, gives the amplification factor and it must be less than or equal to unity for stability.

By neglecting the pressure effects in the induction equation, which is valid in the limit of low beta, the stability analysis can be performed on the induction equation. To further simplify the analysis we consider a uniform magnetic field in the x-direction and only examine parallel propagating modes. This leads to an equation for B_y and B_z and the norm of the two by two matrix of coefficients for the magnetic field determines the stability. We will not produce all the algebra here but merely write the resultant amplification factors and stability criteria.

If we write the induction equation in finite difference form and neglect the Hall term, the amplification factor is given by:

$$|g|^2 = 1 + 4k^4\Delta^4\left(\frac{v\Delta t}{2\Delta}\right)^2\left[\left(\frac{v\Delta t}{2\Delta}\right)^2 - \frac{1}{2}\right] \tag{22}$$

for the Lax-Wendroff scheme and where a constant mean velocity, v is assumed. In the opposite limit we neglect the velocity term and retain the Hall current. This gives an amplification factor:

$$|g|^2 = 1 + 16k^4\Delta^4\alpha^4(4\alpha^2 - \frac{1}{2}) \tag{23}$$

Combining the stability condition $|g|^2 \leq 1$ for the two extreme cases (22) and (23) gives the following constraint on the time step:

$$\Delta t \leq min\left\{\frac{\sqrt{2}\Delta}{(v_A^2 + c_S^2)^{\frac{1}{2}}}, \frac{\sqrt{2}\Delta^2}{2v_A^2/\Omega_i}\right\} \tag{24}$$

which must be satisfied in order for the algorithm to be stable. These constraints can also be obtained from the dispersion relation for the normal modes and substituting the highest frequency mode into $\omega \Delta t < 1$, gives a similar condition.

As will be shown later, the Hall current gives rise to a signifigant splitting of the shear Alfvèn branch into an ion cyclotron wave and whistler mode for wavenumbers $|k| \geq 1$. Since the frequency of the whistler branch increases with the wavenumber while the ion cyclotron becomes constant, it is the whistler mode which generally limits the time step for a low beta plasma. In section 5 a method to remove this constraint and hence investigate the long time behavior of the plasma will be discussed.

3. Tests of the Model

To test the particle MHD algorithm we shall consider the following two cases which both allow for analytical solutions. First, we will show the time evolution of the pure hydrodynamic flow in a shock tube. This test problem involves all salient features of hydrodynamic flow and has been extensively used for testing numerical codes [17,18]. This test case is particularly well suited to check the ability of the numerical scheme to handle discontinuities like shocks and contact discontinuities.

Secondly, we shall examine the dispersion properties of the code, as has been done with earlier versions of the particle MHD model. We discuss here the types of plasma waves which can propagate and their dispersion properties. A comparison of the dispersion of the simulated waves with the actual dispersion of the underlying MHD equations will give us some insight into the effects of finite-sized particles, grid and timestep used in the numerical simulation.

3.1 The Shock Tube Problem

A shock tube is a device used to generate high speed transient flows. It consists of a tube in which two gases at different states, usually with a high pressure ratio, are separated by a diaphragm. When the diaphragm is ruptured at some time, t=0, a complicated flow pattern evolves in the tube. The basic flow pattern is illustrated in Figure 1 by an x-t diagram. At $t \leq 0$ only two thermodynamic states are present in the tube: the high pressure region (4) and the low pressure region (1), separated by the contact discontinuity 'CD'. After rupture of the diaphragm ($t > 0$) a shock wave, denoted by 'S', propagates to the right, beginning at the contact discontinuity. The contact discontinuity now also moves to the right, but at a lower speed than the shock. The region between the shock and the contact discontinuity is indicated by (2). At the same time a rarefaction wave (RW) propagates from the contact discontinuity to the left into the high pressure gas. The region between the contact discontinuity and the tail of the rarefaction wave is denoted by (3).

To solve the problem analytically one has to derive the propagation velocities of the waves and the contact discontinuity as well as the thermodynamic states in the regions (1)-(4) as a function of the initial states. The main parameter is the pressure ratio of the initial state in the two gases p_1/p_4. We will not outline the rather complicated solution here, but refer the reader to Hughes and Brighton [19] and Owczarek [20], where an extensive discussion about the shock tube solutions are given. We also note that there exists an analytic solution for a shock tube with a perpendicular magnetic field [21].

We have run several test cases on the shock tube problem with a 1-D version of the code. The initial values and the numerical parameters are the same for all

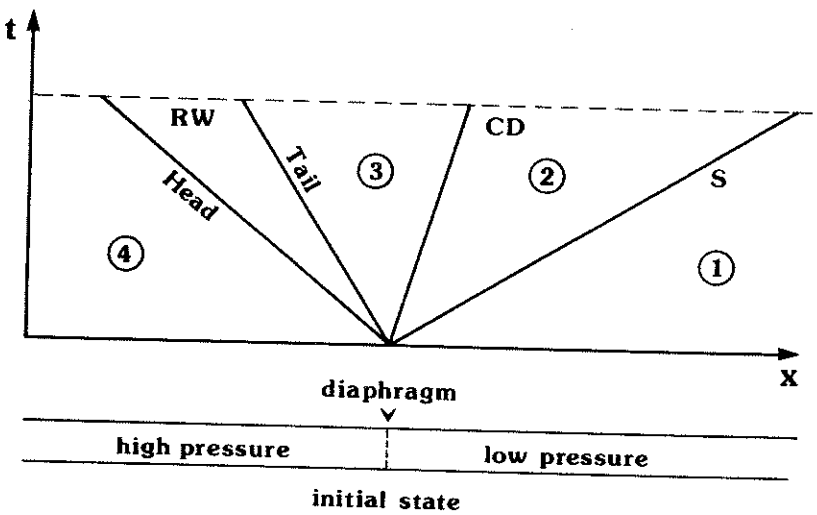

Figure 1. Schematic flow pattern in a shock tube. The x-t diagram shows the propagation of a rarefaction wave (**RW**), a contact discontinuity (**CD**) and a shock (**S**). The gas in the shock tube is characterized by 4 distinct states 1-4.

runs except for the type of viscosity model and the values for the viscosity.

Figure 2 shows the initial values chosen for the tests. In the region $0 \leq x \leq 40$ the gas is at high temperature, density and pressure (T=2, n=2.175, p=4.35) whereas the gas in the rest of the region is at low pressure (T=1, n=0.2175, p=0.2175). The pressure ratio is 40 and both gases have a ratio of specific heats $\gamma = 2$. There are 100 grid points in the simulation box with a total of 2000 particles, distributed according to the densities given above and initially at rest

(actually we used 200 grid points and 4000 particles with periodic boundary conditions, but the left part is not shown). The timestep length was 0.1 normalized units and the runs were done for 200 steps.

Figures 3,4 and 5 show the density, temperature and pressure at the end of the runs. The top panel (a) in each figure shows the exact solution. Panel (b) of each figure shows the solution for a Krook viscosity with $\nu = 1$. The shock is rather sharp, only two grid points wide in the density and pressure and about 3 grid points in the temperature. The shock speed is somewhat lower than in the analytic solution. All variables exhibit the characteristic overshooting and have damped waves behind the shock. This phenomenon has been observed in other numerical schemes for hydrodynamic flow and the excellent review by Sod [17] compares each type. The contact discontinuity is resolved within about 4 grid points in the density and temperature and does not show up in the pressure (what it should not do!). It also seems to be delayed due to the viscosity and is also the case for the rarefaction wave. It should be noted here that the bump in the temperature is resolved very well compared to other methods.

A run with a higher viscosity, $\nu = 5$, is shown in panel (c). Except for very small overshoots at the shock and the contact discontinuity there are no fluctuations visible, and is obviously due to the damping effect of the higher viscosity. The discontinuities are not as sharp as in the former case, but with a thickness of 4 grid points are still very good. A more severe effect is the decrease of the propagation speed of all the discontinuities. This may be best observed with the shock position. The analytical solution shows the shock at x=94 (Figure 4a) whereas the position in Figure 4c is approximately at x=84. Since the shock started at x=40 this means a reduction of the shock speed by

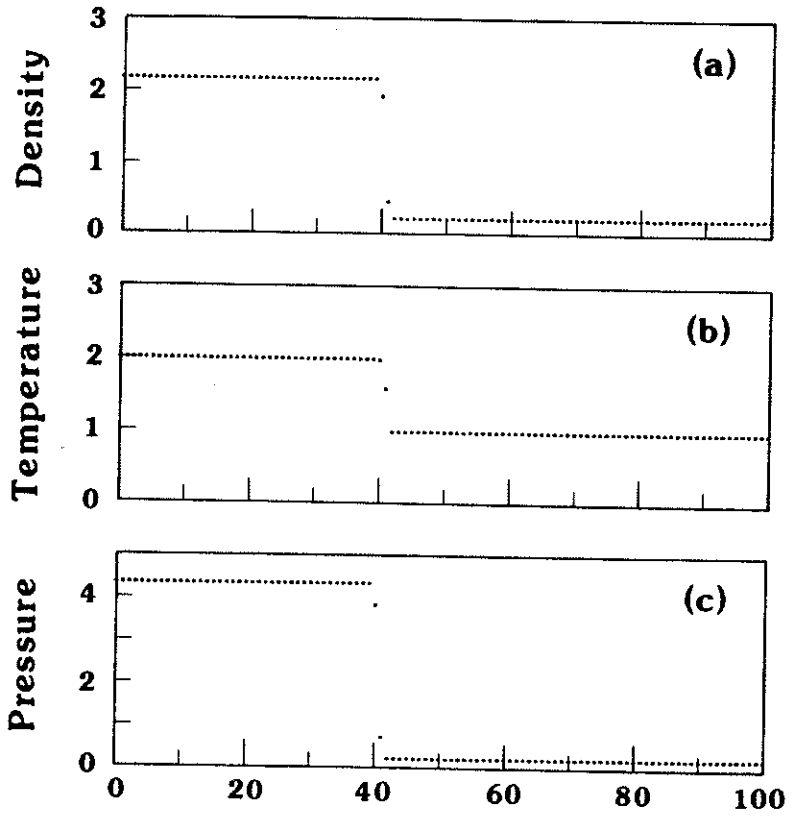

Figure 2. The initial conditions for the shock tube problem. The density ratio is 10, the temperature ratio is 2 and thus the pressure ratio is 40 across the contact discontinuity.

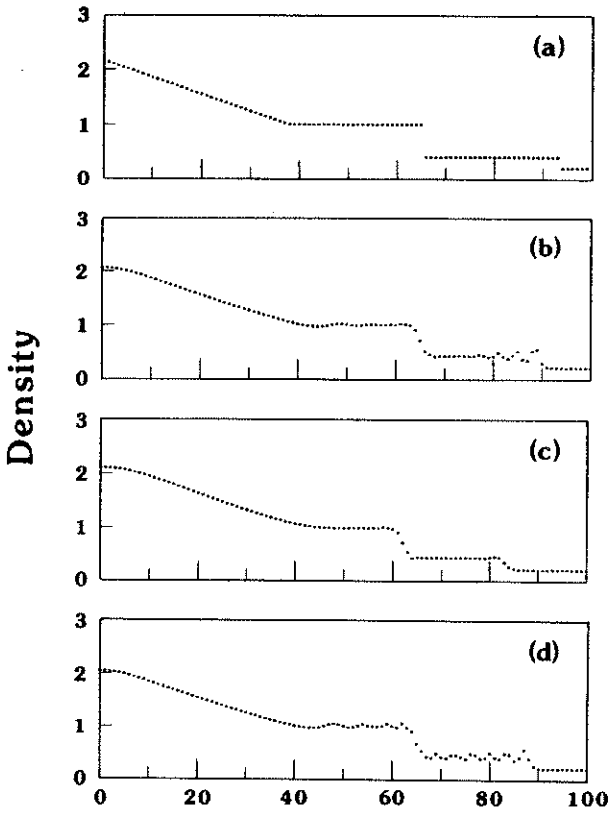

Figure 3. Density variation in the shock tube at t=20.

(a) analytical solution,

(b) Krook viscosity with $\nu_0 = 1$,

(c) Krook viscosity with $\nu_0 = 5$,

(d) Landshoff viscosity with $\nu_0 = 5$.

The right discontinuity is the shock, the left one is the contact discontinuity.

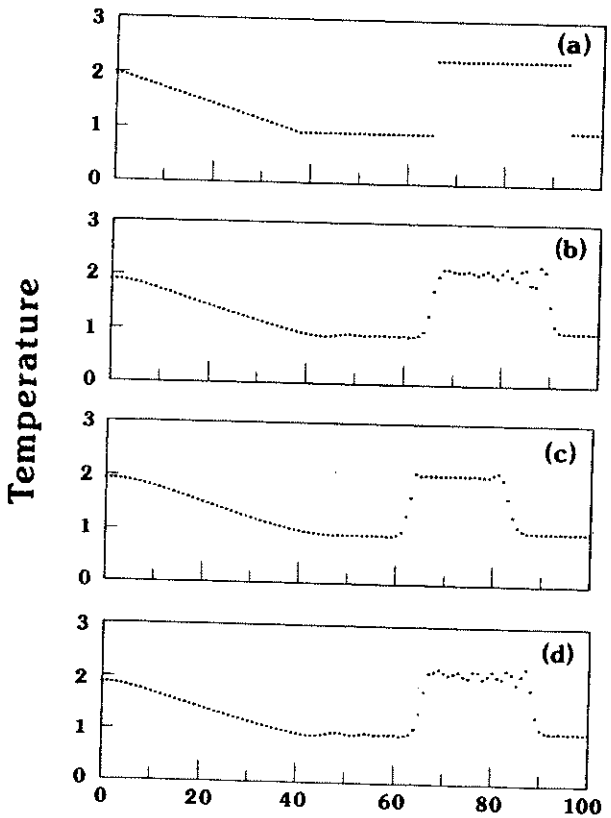

Figure 4. Same as figure 3, but temperature variation.

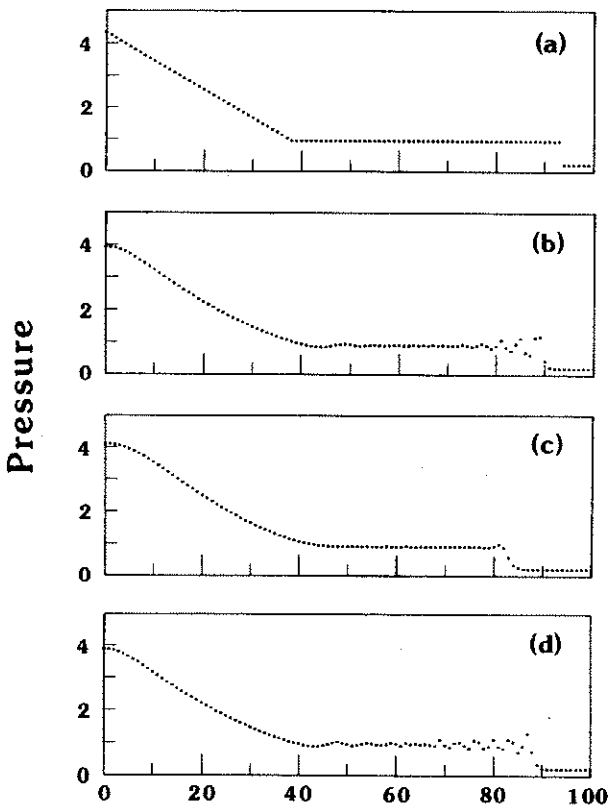

Figure 5. Same as figure 3, but pressure variation.

roughly 20 percent. A similar value is obtained for the contact discontinuity.

Finally, we check if the velocity–dependent Landshoff viscosity can improve the solution. The results of the run are shown in panel (d). We see that the shock is almost delayed as much as in (c). This can be understood as the effect of the high local viscosity in the shock region. Fluctuations behind the shock are still present and only weakly damped. They extend over all the high temperature region between x=65 and x=90. The resolution of the shock and the contact discontinuity is comparable to the simpler Krook viscosity cases. We may therefore conclude that the Landshoff viscosity does not improve the solution of a simulation involving shocks and contact discontinuities.

3.2 Dispersion Properties

In order to derive the dispersion properties of the code let us first outline the dispersion relation of the underlying equations (8). We assume a two dimensional case (x-y) with a uniform ambient magnetic field in the x–direction. We then linearize the equations (8) and Fourier transform them in space and time. Two special cases are considered: waves propagating parallel to the ambient magnetic field, i.e. $k_x \neq 0$, $k_y = 0$, and waves propagating perpendicular to the external magnetic field, i.e. $k_x = 0$, $k_y \neq 0$.

The first case gives basically three different modes. The first is a sound wave with the dispersion relation:

$$\omega = \pm k_x c_s (1 + 3V_T^2/c_s^2)^{\frac{1}{2}} \tag{25a}$$

where $c_s = (\gamma T/m_i)^{\frac{1}{2}}$ means the principal sound speed and V_T refers to the mean random velocity of the finite-size particles. The other modes are Alfvèn

type with the dispersion:

$$\omega = \pm k_x v_A \{z \pm (1 + z^2)^{\frac{1}{2}}\}, \quad z = \alpha k_x / 2 v_A \tag{25b}$$

The outer plus/minus sign refers to forward/backward propagation whereas the inner plus/minus sign refers to an ion cyclotron wave and a whistler wave, respectively. This can be seen in the limit of large wavenumbers, where equation (25b) reduces to:

$$\omega = \omega_{ci}, \quad \omega = \pm k_x^2 v_A^2 / \omega_{ci} \tag{26}$$

for $(k_x v_A/\omega_{ci} \ll 1)$. In the opposite limit $(k_x v_A/\omega_{ci} \gg 1)$ of larger wavelengths we retain the dispersion relation for linear polarized Alfvèn waves in ideal magnetohydrodynamics:

$$\omega = \pm k_x v_A \tag{27}$$

which is also obtained when the Hall parameter, α , vanishes.

In the second case of perpendicular wave propagation the Hall parameter does not affect the dispersion and we obtain the magnetosonic wave:

$$\omega = \pm k_y (c_s^2 + v_A^2)^{\frac{1}{2}} \tag{28}$$

We ran several test cases with a two dimensional version of the simulation model with a uniform plasma and periodic boundary conditions. The box size was 128 times 128 cells with 4 particles per cell. The initial densities and temperatures were uniform. All particles were given an initial random velocity of the order of $0.1 v_o$ in all directions in order to excite the full wave spectrum. The runs extended over 500 time steps with a time step length of $0.1 t_o$. For the simulation runs with the Hall current the value of α was set equal to 6 and for all cases the sound and Alfvèn velocities were 1.42 and 4.26 respectively. To analyze the

dispersion we Fourier transformed the magnetic field components B_x and B_y to k-space and took the time autocorrelation for each (k_x, k_y) mode to obtain the power as a function of frequency ω. Contours of the power spectral density as a function of frequency and wavenumber then clearly displays the wave dispersion.

Figures 6a-d illustrate the wave dispersion obtained from the simulation. Figure 6a shows the case of Alfvèn waves propagating parallel to the ambient magnetic field when the Hall parameter vanishes. The solid circles indicate the analytical solution given by equation (27). The finite width of the branches in the simulation is mainly due to the finite time sample which is being correlated. Since these waves are transverse to the ambient magnetic field, the B_y component was taken for the analysis. The case with finite Hall current is shown in Figure 6b. The Alfvèn branch splits into an ion cyclotron branch (upper curve and solid circles) and a whistler branch (lower curves and open circles) according to the analytic solution expressed in equation (25). Figures 6c and 6d display the transverse propagating magnetosonic waves which are also in agreement with equation (28). As expected the Hall currents do not affect the dispersion of these waves.

In all four cases there is a distinct bending of the branches towards lower frequencies for wavenumbers $|k| \geq 1$. A detailed analysis shows that this effect is due to the finite particle size and the finite differencing. Different particle weigthing schemes and finite differencing have been tested and it turns out the method outlined in section 2 is the optimal with respect to dispersion properties, computational efficiency and the ability to treat complex boundary conditions and irregular grids. Inspection of Figure 6 indicates the bending of the branches occurs roughly at $|k| = 1$. Since the maximum wavenumber in the system is π we

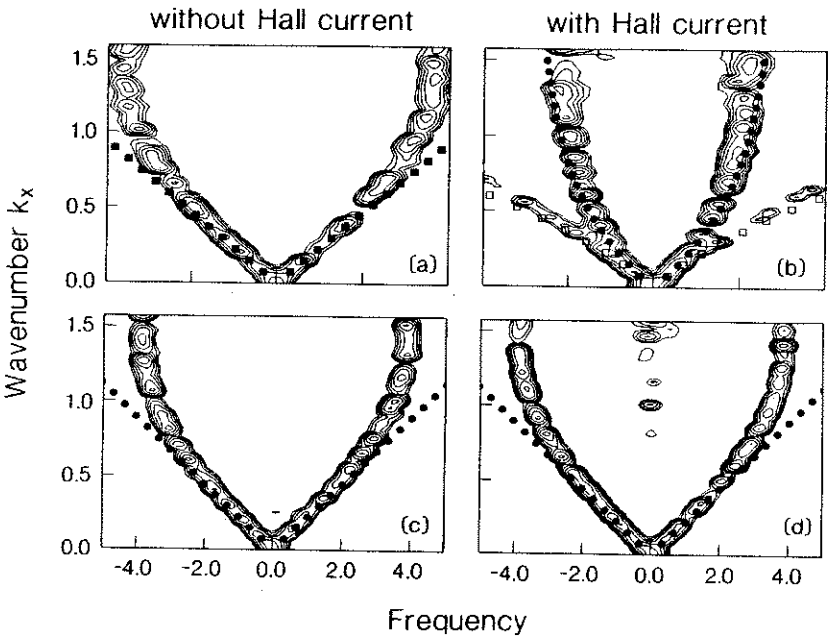

Figure 6. **(a)** Contours of the power spectral desity versus ω and k_x of the magnetic field component B_y. There is no Hall current, thus the dispersion of Alfvèn waves is exhibited. Solid dots indicate the analytical solution.

(b) Same as (a) but with finite Hall current. The Alfvèn branches split into branches of ion cyclotron (upper curves, solid dots) and whistler waves (lower curves, open dots).

(c) Contours of the power spectral density versus ω and k_y of the magnetic field component B_x. There is no Hall current and the curves show the dispersion of magnetosonic waves. Solid dots indicate the analytical solution.

(d) Same as (c) but with finite Hall current.

may therefore conclude that the code describes wave propagation correctly up to wavenumbers of about one third of the maximum wavenumber of the system. This observation is also consistent with the previously estimated shock thickness of about 3-4 grid points.

Understanding the strengths and shortcomings of the model we may now proceed to apply it to a problem of current interest, namely the interaction of a comet with the solar wind plasma where all of the previously discussed plasma-physical processes play an important role.

4. Simulation of the Interaction of the Solar Wind with a Comet

Recently there has been a strong interest in the study of comets and their interaction with the solar wind. This may be due to the 1986 appearance of comet P/Halley and the 'visit' of 5 spacecraft, providing detailed experimental information about the complex interaction of most parts of the cometary coma with the solar wind. In view of these new experimental results as well as earlier observations and theoretical work, it turns out that the comet interaction is one of the most complex among all solar system bodies and exhibits some unique features [15,22,23,24]. Even though the experimental data increased our knowlege and understanding dramatically, certain gaps persist. Spacecraft can only take a snapshot, very restricted in space and time, of their object, so that the extrapolation of data to the global interaction may be ambiguous, as may be the distinction of spatial and temporal structures. In order to interpret experimental results and to understand the underlying physical processes one has to construct models of the physical processes involved. Due to the complexity of the interactions and their nonlinearity, simulation studies using the basic equations are well suited to cope with the problem. They offer us the ability to vary parameters and

test their influence on the interaction process. The 5 spacecraft at P/Halley each encountered the comet at a different time and made quite different observations, indicating that the comet and solar wind are varying rapidly in time. We therefore have quite a volume of experimental data available to serve both as input parameters and as restrictions for a model. In the following, we will outline the configuration of a global cometary model employing the particle MHD approach and present some preliminary results.

4.1 Basic Physical Processes

A comet can be viewed as a source of neutral gas in the solar wind. Due to the negligible gravitational acceleration of the cometary nucleus, evaporating cometary gas, predominantly H_2O vapor, streams off the nucleus uniformily in all directions. This forms an extended neutral atmosphere which is collisionless except for the innermost part of the coma where collisions and related chemical reactions play an important role [22,25]. This latter region will not be considered here. Due to various mechanisms that may ionize neutrals of the cometary atmosphere, such as photoionization and charge exchange, among others, complex interactions begin with the solar wind. As soon as a neutral is ionized it interacts with the solar wind electric and magnetic field. This interaction is commonly called 'pick-up' of cometary ions, although it may not directly lead to the assimilation of the newborn ion to the solar wind, depending on the angle θ between the solar wind bulk flow velocity and the solar wind magnetic field [26]. For $\theta = 90^o$ the ion will be accelerated by the solar wind motional electric field within about one gyroperiod and its guiding center will then move with the solar wind bulk flow speed while it gyrates with the same velocity. In the other extreme case, $\theta = 0^o$, there is no interaction of a single ion but an ensemble of ions constitutes

a cold ion beam in the solar wind frame of reference, which may be unstable and lead to the coupling of newly born ions with the solar wind by wave-particle interactions [27,28,29].

A more general treatment shows that, neglecting the small motion of the neutrals and averaging over the gyromotion, newborn ions will drift perpendicular to the magnetic field with a velocity $v_D = v_{SW} sin\theta$. Equivalently, seen in the bulk flow frame of reference there is a drift along the field lines with a velocity $-v_{SW} cos\theta$, v_{SW} being the velocity of the solar wind [26,27]. Clearly these newborn ions constitute a highly nonmaxwellian velocity distribution, namely a ring in velocity space. In order to treat pickup ions as a fluid we have to describe them by thermodynamic variables. Definitions for their density and velocity are clear and a temperature may be defined by the kinetic energy of the gyromotion, i.e. $W = \frac{1}{2} m v_{SW}^2 sin^2\theta$. This approach, implying a isotropic pressure is partly justified by the fact that the pickup ions experience rapid pitch angle scattering due to instabilities and fluctuations of the magnetic field. This result has been derived from theoretical considerations [28] and has also been confirmed with recent experimental results [24]. Henceforth, we will assume that newborn ions are assimilated into the solar wind on time scales short compared to MHD time scales and the initial temperature is given by the kinetic energy of the gyromotion. We consider a more sophisticated description in section 5.

The pickup of heavy cometary ions, predominantly of the water group (HO^+, H_2O^+, H_3O^+ and CO^+) causes the supersonic solar wind to be massloaded and thus decelerated. It has been shown that a small contamination with heavy pickup ions on the order of one percent in number density, is sufficient to brake the flow and give rise to the formation of a bow shock [30]. Unlike planetary

shocks it is not formed by an obstacle in the solar wind flow, hence we may expect a different structure for the cometary bow shock. The shock will further decelerate, heat and diverge the flow. Rough estimates predict the subsolar point of the bow shock to be located $10^5 - 10^6$ km upstream of the nucleus. For the GIOTTO encounter with comet P/Halley it was found to be 3.9×10^6 km. Downstream of the bow shock there extends a magnetosheath where the solar wind flow gets more massloaded, further decelerated and is cooled by new pickup ions since these ions cannot gain much kinetic energy any further in the rather slow bulk velocity. The magnetic field, frozen into the flow, is draped and 'piles up', becoming about ten times its interplanetary value. Very close to the nucleus the outflow velocity of the neutral gas and therfore of the fresh ions, becomes important and a cometary ionosphere is formed. The radius of the ionosphere is of the order of a few thousand kilometers and will not be resolvable in our model. Another problem arises with the ionosphere in a two dimensional simulation and is due to the fact that the flow stagnates at the ionopause and the magnetic field cannot penetrate it, thus piling up at the subsolar point. In reality the field lines slip over the ionosphere in the third dimension. In our two dimensional simulations we avoid the stagnation of the flow and allow the magnetic field to slip through. There have been other distinct boundaries observed during the recent missions [24], but their physical nature is still unclear and it is not known whether they are unique or just transient features. Simulations may help to bring some insight here.

4.2 Model Configuration

Knowing the physical processes described in the previous section, we may now establish the numerical model. In particular we will have to prescribe proper

boundary conditions and find a suitable implementation of the mass loading process. Figure 7 gives an overview of the simulation configuration. The cometary nucleus is located at the center of the simulation box which extends over 128×128 gridpoints or 4×10^6 km in each direction. The solar wind streams in from the left side across boundary A. In order to generate a steady flow new particles are created here at every time step [16]. All quantities are fixed at this boundary and the inflow velocity is taken to be 5 (normalized units) while the Alfvèn and sound speed are 1. and 1.42, respectively. The other boundaries B,C and D are not as easy to treat. Since values are not known here we require that their normal derivatives vanish. This treatment is sometimes referred to as an 'open' boundary [31]. In fact, it turns out from the simulation results that it is not completely open since waves are partly reflected there. Unfortunately, there is no natural and physically meaningful choice for these three boundaries. Of course particles crossing these boundaries are removed. The ambient magnetic field, carried by the solar wind, is chosen to be in the y-direction although the model allows for any configuration as long as the divergence of the magnetic field vanishes.

We implemented the mass loading process by creating new (cometary) particles at every time step, although other ways are possible such as adding mass, momentum and internal energy to the solar wind particles. To determine the rate at which particles are created in each cell we used the simple, but for our purpose sufficient, model of Haser [32] which is:

$$q = \frac{Q_o m_i e^{-r/\lambda}}{4\pi r^2 \lambda} \tag{29}$$

where Q_o is the production rate of cometary neutrals (molecules/second), m_i is the average mass of cometary ions, r is the distance from the nucleus and λ is the

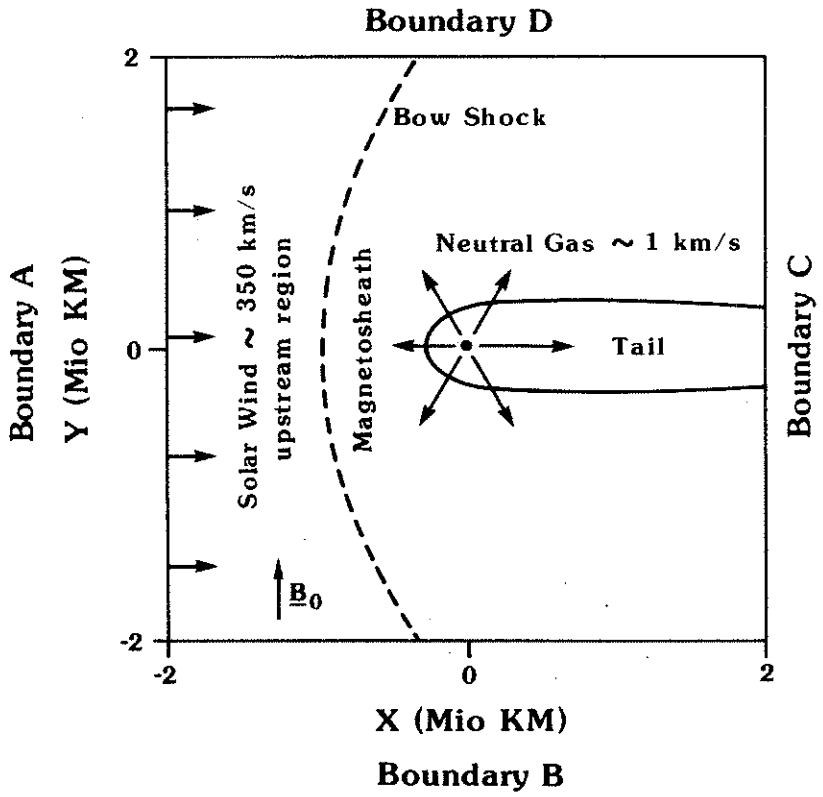

Figure 7. Sketch of the solar wind - comet interaction. The box used for the simulations as well as some cometary features are schematically indicated.

photoionization scale length. This model takes into account the radial outflow of neutrals at a constant velocity as well as their destruction and the creation of new ions due to photoionization. A more sophisticated model would distinguish between different ion species and deal with other ionization processes as well. Equation (29) may be rewritten in normalized units and gives the rate at

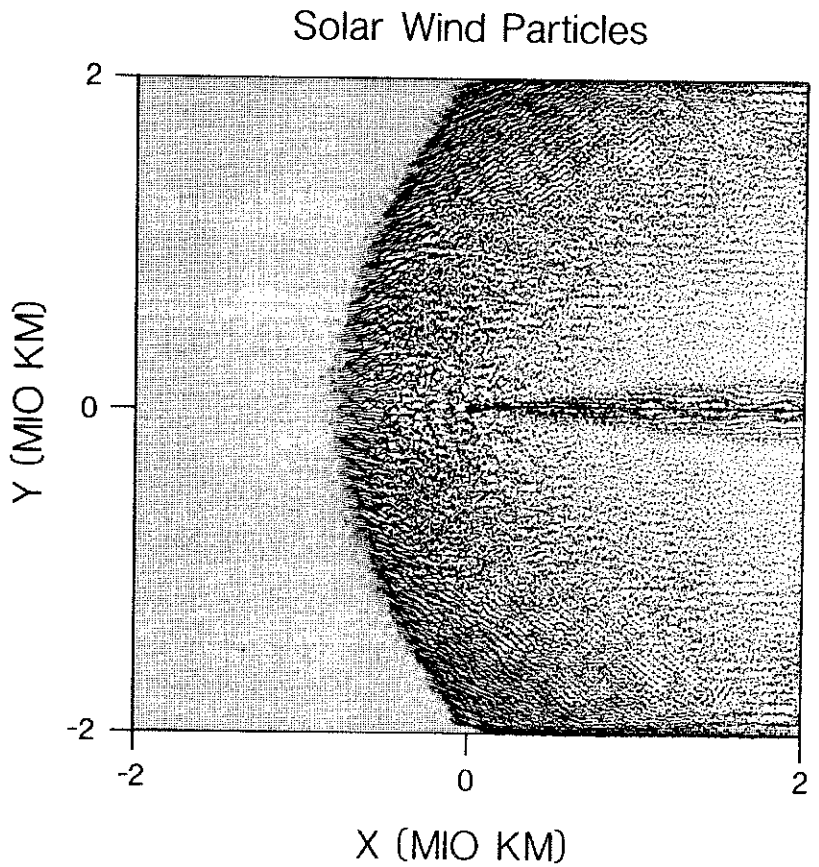

Figure 8. Solar wind particles at t=150. The dark spot in the center of the box indicates the position of the nucleus. The bow shock is clearly visible as well as MHD waves and turbulence downstream of the shock.

which new particles are to be created within every time unit and cell which is equivalent to the probability of a unit particle being created. Since the numerical scheme becomes computationally expensive with number of particles, we have to compromise between computational cost and smooth loading with new particles. Therefore, we create a new particle or fluid element only when the probability in a given cell exceeds a threshold and we will limit the particle creation close to the center thereby avoiding the singularity in equation (29).

In this way there will be only a few particles in the foreshock region and many close to the nucleus but the results show that this method of particle loading works well. In addition to these considerations we also have to randomize the particle creation carefully in space and time in order to avoid transient features in the results.

4.3 Simulation Results

A typical simulation run of the comet interaction produces an enormous amount of data. We will therefore show only some of the aspects of a particular set of simulations. Besides other parameters given above we match the dimensionless parameters to the following for a comet:

$$Q_o = 4 \times 10^{29} \quad molecules \quad per \quad second$$

$$\lambda = 5 \times 10^5 \quad km$$

$$m_i = 18 \quad amu$$

and for the solar wind:

$$\rho_{SW} = 10 \times 10^6 \quad amu/m^3$$

$$c_{s,SW} = 100 \quad km/sec$$

$$v_{A,SW} = 70 \quad km/sec$$

$$B = 10 \quad nT$$

Therefore, the mesh size corresponds to 31250 km and a time step is equivalent to 312.5 seconds. The simulation is run for 1500 timesteps ($\Delta t = 0.1 t_o$) corresponding to 13 hours in real time. We took the value of the Krook viscosity parameter here as $\nu_0 = 0.5$. At the end of the run a quasi-stationary state is reached. The stationary state is indicated by the fact that the net number of particles in the simulation domain ceases to increase. At this time the bow shock, which started to develop early in the run, has flared out and moved upstream to its final position. All other parameters, like the magnetic field, density and velocity are stationary besides distinct fluctuations. Figure 8 shows a plot of the solar wind particles only. The bow shock is clearly visible and rather sharp. Upstream, the solar wind particles are highly ordered and only few fluctuations are visible. Downstream, the particles are more clustered, indicating wave activity. The particle density increases rapidly across the shock and inspection of the temperature also shows a jump in the internal energy. In the upper and lower right corners of the simulation domain we observe weak wave structures which are standing. They are attributed to boundary effects and are excited by incident downstream fluctuations.

Figure 9 shows the population of cometary particles. Again, the bow shock is visible, this time due to trapped particles there. The shock creates large fluctuations in its vicinity, both in the magnetic field and in the pressure. These fluctuations enhance the density by a type of trapping but this process needs further investigation. In the vicinity of the nucleus we see the formation of a dense and cold inner coma. The flow, which may also be seen in Figure 10, slows

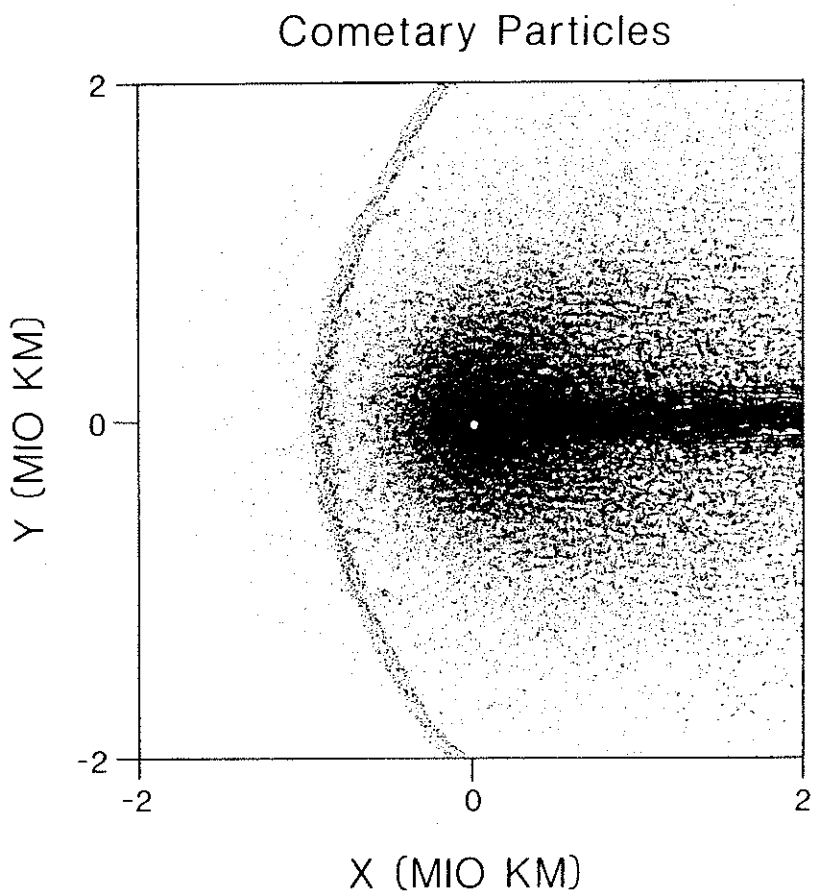

Figure 9. Cometary particles corresponding to figure 8. Note that different particles carry different densities, thus the density of dots corresponds only roughly to real densities. A dense inner coma and tail are visible together with trapped particles along the bowshock.

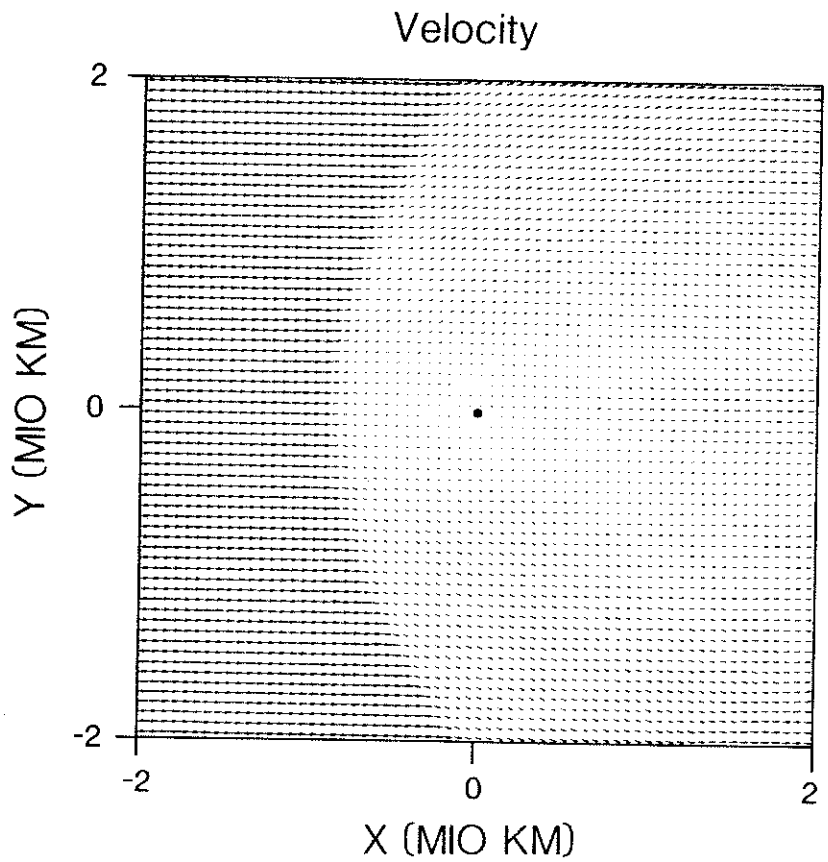

Figure 10. Vectors of the velocity at the gridpoints, decimated by 2 in each direction, thus only every fourth vector is displayed.

down and almost stagnates at the nucleus, but passes through at about $0.4v_o$. We also observe in Figure 10 the strong deflection of the flow when it passes the bow shock. The magnetic field increases across the bow shock by a factor of 3 and gets deflected. Further downstream the field lines hang up in the decelerated flow and get strongly draped around the nucleus, but slip through. Downstream from the nucleus an ion tail is formed, and is characterized by a cold and dense plasma as well as two lobes with oppositely polarized magnetic fields. Due to the fact that the field lines slip through the nucleus, there remains a finite z-component of the magnetic field and there is no neutral line.

Putting these results together we may conclude that the particle MHD approach is well suited to simulate the interaction of the solar wind with a comet. At a first glance there appears no improvement over other approaches [14,15] but there is plenty of room to extend the description of the plasma behavior. The present model sustains waves of various nature and we must analyze the excitation and propagation. By treating the fluid elements as particles we may distinguish cometary from solar wind plasma and thus we are able to examine differential motion of both plasmas. This will require a multifluid description of the plasma which we will briefly outline in the next section together with some other possible extensions.

5. Further Extensions

5.1 The Particle MHD Approach with Multiple Ion Species and Massless Electrons

In this section we consider the extension of the particle MHD code to treat multiple ion species. We assume that for each ion species there belongs one electron population. We will then combine them to obtain magnetofluid equations

for every ion population together with its electrons. These equations can then in turn be combined to give an Ohm's law and a magnetic induction equation for the bulk fluid. Let α indicate the different ion and electron constituents. We may then write the equations of continuity, momentum and energy conservation for every constituent as follows [6,10]:

$$\frac{\partial n_\alpha}{\partial t} + \vec{\nabla}(n_\alpha \cdot \vec{v}_\alpha) = 0 \tag{30a}$$

$$m_\alpha n_\alpha \frac{d\vec{v}_\alpha}{dt_\alpha} = -\vec{\nabla}p_\alpha + q_\alpha n_\alpha(\vec{E} + \frac{1}{c}\vec{v}_\alpha \times \vec{B}) \tag{30b}$$

$$\frac{dT_\alpha}{dt_\alpha} = -(\gamma_\alpha - 1)T_\alpha \vec{\nabla}\vec{v}_\alpha \tag{30c}$$

where n_α, m_α, $\vec{v}_\alpha$, p_α, q_α, T_α, and γ_α denote the constituents number density, particle mass, velocity, partial pressure, particle charge, temperature and ratio of specific heats, respectively. We defined the partial pressure and the temperature with respect to the species mean velocity $\vec{v}_\alpha$, thus there appear no transport terms due to a drift of a constituent relative to the bulk flow of the whole fluid. The convective derivative is therefore also defined by the species velocity rather than the bulk flow velocity:

$$\frac{d}{dt_\alpha} = \frac{\partial}{\partial t} + (\vec{v}_\alpha \cdot \vec{\nabla})$$

This description fits nicely into the concept of fluid particles. The continuity equation will be resembled by the trajectories of the particles, which will be of either species. Any transport of momentum and internal energy (heat) is accomlpished by the motion of distinct particles, thus there is no need to describe it as a diffusion process. Equations (30) describe that the coupling between the different constituents occurs only via the self consistent electric and magnetic fields $\vec{E}$ and $\vec{B}$. Collisional coupling between the different species may also be included

by adding appropiate collision terms to the right hand sides of equations (30). We close the equations (30) by specifying an equation of state:

$$p_\alpha = n_\alpha \cdot T_\alpha \tag{31}$$

and the Maxwell equations:

$$\vec{\nabla} \cdot \vec{B} = 0 \tag{32}$$

$$\vec{\nabla} \times \vec{E} = -\frac{1}{c}\frac{\partial \vec{B}}{\partial t} \tag{33}$$

$$\vec{\nabla} \times \vec{B} = \frac{4\pi}{c}\vec{j} \tag{34}$$

where $\vec{j}$ is the total current.

The next step is to combine the electrons and ions of one species to obtain the fluid equations which no longer contain the charge explicitly. We assume quasineutrality ($n_{se} \simeq n_{si} = n_s$) and neglect all terms of the order of m_{si}/m_e. For the quasineutral equations we denote a species now by the subscript s. By adding the respective momentum equation (30) for an ion and corresponding electron constituent we obtain the species momentum equation [8]:

$$m_s n_s \frac{d\vec{v}_s}{dt_s} = -\vec{\nabla}p_s + \frac{1}{c}\vec{j}_s \times \vec{B} \tag{35}$$

where:

$$m_s = m_{si} + m_{se} \simeq m_{si}$$

$$\vec{v}_s = (m_{se}\vec{v}_{se} + m_{si}\vec{v}_{si})/m_s \simeq \vec{v}_{si}$$

$$\vec{j}_s = en_s(\vec{v}_{si} - \vec{v}_{se})$$

$$p_s = p_{si} + p_{se}$$

Similarly by multiplying the electron momentum equation by the ion mass and vice versa and subtracting these two we obtain an equation for the species

current:

$$n_s m_e \frac{d\vec{j}_s}{dt_s} = \vec{\nabla} p_{se} + n_s e(\vec{E} + \frac{1}{c}\vec{v}_s \times \vec{B}) - \frac{1}{c}\vec{j}_s \times \vec{B} \qquad (36)$$

Equation (36) may be viewed as a 'partial' Ohm's law for species s. For most applications we may neglect the left hand side and the electron pressure, hence:

$$n_s e(\vec{E} + \frac{1}{c}\vec{v}_s \times \vec{B}) - \frac{1}{c}\vec{j}_s \times \vec{B} = 0 \qquad (37)$$

Adding (37) for all species gives us an equation for the electric field:

$$\vec{E} = -\frac{1}{c}\vec{v} \times \vec{B} + \frac{1}{enc}\vec{j} \times \vec{B} \qquad (38)$$

which in turn may be combined with (33) and (34) to yield an equation for the magnetic field:

$$\frac{\partial \vec{B}}{\partial t} = \vec{\nabla} \times \left\{ \vec{v} \times \vec{B} + \frac{c}{4\pi ne}\vec{B} \times (\vec{\nabla} \times \vec{B}) \right\} \qquad (39)$$

The essential difference between equations (38) and (39) and a single fluid description is the definition of $\vec{v}$:

$$\vec{v} = \sum_s n_s \vec{v}_s / n \quad , \qquad n = \sum_s n_s \qquad (40)$$

which states that the magnetic field lines do not move (in the absence of Hall currents) with the bulk mass velocity, but rather with a bulk number velocity. The two descriptions only coincide in the case of a unique ion mass, a condition that is strongly violated in the case of solar wind - comet interaction. This result was also pointed out by Marochnik [33].

With the help of equations (37) and (38) we may now rewrite the species momentum equation (35) as:

$$\frac{d\vec{v}_s}{dt} = -\frac{1}{m_s n_s}\vec{\nabla} p_s - \frac{1}{4\pi n m_s}\vec{B} \times (\vec{\nabla} \times \vec{B}) - \vec{\Omega}_s \times (\vec{v}_s - \vec{v}) \qquad (41)$$

with the vector of the gyrofrequency: $\vec{\Omega}_s = e\vec{B}/m_s c$. Equation (41) differs significantly from a single fluid description. Normalizing the magnetic field in (41) gives different Alfvèn velocities for each species:

$$v_{A,s}^2 = B_0^2/4\pi n m_s \qquad (42)$$

It is at a first glance surprising that the total number density appears in (42) instead of the species number density. It becomes clear however, when one recalls that this term stems from the part of the cross electric field which is due to the total current (38). The last term in equation (41) is completely new compared with the single fluid equation. First, we note that it vanishes when either the species velocity equals the bulk velocity or when the drift velocity ($\vec{w}_s = \vec{v}_s - \vec{v}$) is parallel to the magnetic field. The term resembles a gyromotion very similar to that of pick up ions (see section 4). Of course we are not interested in this fast timescale. Let us therefore assume that the bulk velocity $\vec{v}$ changes only little over one gyroperiod and that the first two terms on the right hand side of equation (41) change $\vec{v}_s$ only little compared to the last term, i. e. the last term dominates ($|\vec{\Omega}_s \times \vec{w}_s| \ll (k^2 v_{A,s}^2, k^2 c_s^2)$, where k is a typical wavenumber and c_s the species soundspeed). We may then average the last term over a gyroperiod, the result of which is, that the component of the drift velocity perpendicular to the magnetic field vanishes, i. e.:

$$w_{s\perp} = 0 \qquad (43)$$

This result resembles the fact, that in an ideally conducting fluid (single or multiple species) the ions are tied to the fieldlines, i. e. there is no drift perpendicular to the field in the absence of cross–field pressure gradients and field inhomogenities [34]. Thus any cross field motion is adjusted to the motion of the field on

the timescale of a gyroperiod. In the particle MHD approach we may accomplish this by replacing the last term in (41) by an appropriate drag term, effective only perpendicular to the field. As for any drag term we have to take care that the total momentum change induced by this term vanishes at least locally. This means that within one cell and assuming that the bulk velocity and the magnetic field direction is constant over a cell, the drag terms cancel each other. This requires that the drag constant takes different values for each species, namely:

$$\nu_k = \frac{\nu_0}{m_k} \tag{44}$$

where ν_0 is a reference drag term, i. e. the drag term for the lightest ion species with $m_k = 1$. Equation (44) together with (45) then also expresses the fact, that the heavier the ions, the less they are tied to the fieldlines. The normalized momentum equation for a particle k reads then:

$$\frac{d\vec{v}_k}{dt} = -\frac{1}{m_k n_s}\vec{\nabla}p_s - \frac{v_A^2}{v_0^2 n m_k}\vec{B}\times(\vec{\nabla}\times\vec{B}) - \nu_k\{\vec{v}_k - \vec{v} - (\vec{b}:\vec{b})\cdot(\vec{v}_k - \vec{v})\} \tag{45}$$

Due to the presence of multiple species we have now a different normalization, i. e. $v_0^2 = T_0/m_0$, $v_A^2 = B_0^2/(4\pi n_0 m_0)$ and $\vec{b} = \vec{B}/|\vec{B}|$ is a unit vector parallel to the magnetic field. The drag constant, ν_0, should be of the order of the gyrofrequency but not exceed unity.

The full set of equations is then given by (8a), (45), the unchanged energy equation:

$$\frac{dT_k}{dt} = -(\gamma_k - 1)T_k\vec{\nabla}\vec{v}_s \tag{46}$$

and equation (39) for the magnetic field.

Due to the presence of a distinct sound and Alfvèn speed for each species and to the coupling term in (45) we expect a complicated wave spectrum for the above

model. Wave modes of the different fluids may couple by virtue of the magnetic field and the explicit drag term. In particular the case of counterstreaming plasma along field lines is expected to be highly unstable and should lead to the excitation of magnetohydrodynamic waves. These and other properties of the multifluid particle MHD model are currently being investigated.

5.2 Semi–implicit Particle MHD Algorithm

From the previous analysis it has been shown that the introduction of the displacement current in the induction equation (8e), introduces high frequency wave modes in the simulation model. For the induction equation (8e) this added a higher frequency whistler mode and equation (41) added an additional Alfvèn branch. The appearence of these modes may severely constrain the time step (see equation (24)) used in the simulation and therefore a procedure to overcome this limitation should be introduced.

A possible solution to the time step problem in the particle MHD model is to use the semi–implicit method for eliminating the fast mode time step constraint. This method has been used in fluid dynamics [35] and recently has been introduced in codes for solving the resistive MHD equations [36]. In this section we briefly outline the procedure and show how it can be applied to the induction equation for eliminating the shear mode time step constraints which arise from the Hall current.

As a simple illustration of the technique we consider a one dimensional parabolic partial differential equation:

$$\frac{\partial u}{\partial t} - K\frac{\partial^2 u}{\partial^2 x} = 0 \tag{47}$$

This equation may be advanced in time using an explicit first order scheme,

written as:

$$u_j^{n+1} = u_j^n + \frac{K\Delta t}{\Delta x^2}(u_{j+1}^n - 2u_j^n + u_{j-1}^n) \tag{48}$$

This method is stable and first order accurate for $\Delta t < \Delta x^2/2K$. In order to remove the time step restriction we simply approximate the terms producing the mode and subtract them from each side of the partial differential equations. Therefore the following equation results:

$$u_j^{n+1} - \frac{K_0\Delta t}{\Delta x^2}(u_{j+1}^{n+1} - 2u_j^{n+1} + u_{j-1}^{n+1}) =$$

$$u_j^n + \frac{K\Delta t}{\Delta x^2}(u_{j+1}^n - 2u_j^n + u_{j-1}^n) - \frac{K_0\Delta t}{\Delta x^2}(u_{j+1}^n - 2u_j^n + u_{j-1}^n) \tag{49}$$

where K_0 is an arbitrary constant. The equation is now solved by evaluating the terms on the right explicitly, where all quantities are known and solving then the Helmholtz type equation for the quantities of the left hand side at the new timestep. The method is particularly useful because K may be a function of position and the form of the semi–implicit term can be choosen arbitrarily. A stability analysis gives an amplification factor as: $g = 1-(1+2K\Delta t)/(1+4K_0\Delta t)$ and from the condition $|g| \leq 1$, this leads to an unconditionally stable scheme for $K_0 \geq K/2$ and arbitrary Δt.

We now show how the semi–implicit method may be implemented in the Lax–Wendroff scheme for the induction equation. The time differenced form of this equation is given as:

$$\vec{B}^{n+1/2} =< \vec{B}^n > + \frac{\Delta t}{2}\vec{\nabla} \times (\vec{v}^n \times \vec{B}^n) \tag{50a}$$

$$\vec{B}^{n+1} = \vec{B}^n + \Delta t\vec{\nabla} \times (\vec{v}^{n+1/2} \times \vec{B}^{n+1/2}) + \alpha\Delta t\vec{\nabla}\times\left\{\frac{\vec{B}^n}{n^n} \times (\vec{\nabla} \times \vec{B}^n)\right\} \tag{50b}$$

where we have made the Hall term accurate to first order for simplicity. A semi–implicit form of equation (50b) is:

$$\vec{B}^{n+1} - \alpha_0\Delta t\nabla^2\vec{B}^{n+1} = \vec{B}^n +$$

$$\Delta t\vec{\nabla} \times \{\vec{v}^{n+1/2} \times \vec{B}^{n+1/2}\} + \Delta t\vec{\nabla}\times\left\{\frac{\alpha\vec{B}^n}{n^n} \times (\vec{\nabla} \times \vec{B}^n)\right\} - \alpha_0\Delta t\nabla^2\vec{B}^n \tag{51}$$

and the operator is chosen such that it only marginally affects the long wavelength modes but attenuates the short wavelengths in order to allow for larger time steps. The value of the constant, α_0, is determined by performing a stability analysis on the linearized form of equation (51). Assuming $\vec{B} = B_0\vec{e}_z$ and considering only parallel propagating modes ($k_x \neq 0$, $k_y = 0$) equation (51) becomes:

$$\vec{B}_y^{n+1} - \alpha_0\Delta t\frac{\partial^2}{\partial^2 x}\vec{B}_y^{n+1} = \vec{B}_y^n + \alpha\Delta t\frac{\partial^2}{\partial^2 x}\vec{B}_z^n - \alpha_0\Delta t\frac{\partial^2}{\partial^2 x}\vec{B}_y^n \tag{52a}$$

$$\vec{B}_z^{n+1} - \alpha_0\Delta t\frac{\partial^2}{\partial^2 x}\vec{B}_z^{n+1} = \vec{B}_z^n - \alpha\Delta t\frac{\partial^2}{\partial^2 x}\vec{B}_y^n - \alpha_0\Delta t\frac{\partial^2}{\partial^2 x}\vec{B}_z^n \tag{52b}$$

where we have neglected the velocity term in order to simplify the analysis. Replacing the spatial finite difference operator by $K = -4sin^2(k\Delta x/2)/\Delta x^2$ we can write equation (52) in the form of a matrix equation:

$$\vec{u}^{n+1} = \mathbf{A}\vec{u}^n$$

where $\mathbf{A}$ is the amplification matrix and $\vec{u}^T = (B_z, B_y)$. The eigenvalues of matrix $\mathbf{A}$ are computed and the amplification factor g is given by:

$$(1 - \alpha_0 K\Delta t)g = \frac{1}{2} - K\alpha_0\Delta t \pm Ki\alpha\Delta t \tag{53}$$

Unconditional stability with respect to the shear Alfvèn branch holds provided the condition:

$$\alpha_0 \geq -\alpha^2 K\Delta t + \frac{3}{4K\Delta t} \tag{54}$$

is satisfied.

It should be noted here that even though the numerical scheme may be stable it could be inaccurate. Excitation of fluctuations at small scales would remain as undamped noise for any value of the time step. In order to make the scheme accurate to higher order it is found that applying the semi-implicit operator to both steps of the Lax-Wendroff scheme significantly improves the accuracy. Therefore we obtain an accurate solution at almost all scales using:

$$\vec{B}^{n+1/2} - \alpha_0 \frac{\Delta t}{2} \nabla^2 \vec{B}^{n+1/2} = < \vec{B}^n > +$$

$$\frac{\Delta t}{2} \vec{\nabla} \times \{\vec{v}^n \times \vec{B}^n\} + \alpha \frac{\Delta t}{2} \vec{\nabla} \times \left\{ \frac{\vec{B}^n}{n^n} \times (\vec{\nabla} \times \vec{B}^n) \right\} - \alpha_0 \frac{\Delta t}{2} \nabla^2 \vec{B}^n \qquad (55a)$$

$$\vec{B}^{n+1} - \alpha_0 \Delta t \nabla^2 \vec{B}^{n+1} = \vec{B}^n + \Delta t \vec{\nabla} \times \{\vec{v}^{n+1/2} \times \vec{B}^{n+1/2}\} +$$

$$\alpha \Delta t \vec{\nabla} \times \left\{ \frac{\vec{B}^{n+1/2}}{n^{n+1/2}} \times (\vec{\nabla} \times \vec{B}^{n+1/2}) \right\} - \alpha_0 \Delta t \nabla^2 \vec{B}^{n+1/2} \qquad (55b)$$

as the difference scheme.

The form of the semi-implicit operator is quite arbitrary and it may be a function of space. This is important for problems where large spatial variations in the propagation speed of the high frequency mode occur in the simulation domain. A discussion of this procedure as well as further details of the numerical scheme will be published elsewhere.

6. Conclusions and Summary

The investigation of collective plasma behavior in the MHD regime using a particle approach, which is inherently Lagrangian, is shown to be flexible enough to attack a wide range of physical problems. Algorithms which allow solutions of the equations of motion to second order accuracy in space and time have

been implemented and extensively tested. These include the leapfrog method for advancing the positions and velocities of the particles or fluid elements, the Lax-Wendroff scheme for advancing the magnetic field on the mesh, and an area weighting method using a two grid system for interpolation of particle quantities to grid points and vice versa.

Tests of the model have shown it is accurate enough to resolve shocks and discontinuities and using a model shock tube problem, where an analytic solution is possible and most fluid codes are checked against, it is shown to perform as well as most other models. The particle MHD model allows for flexibility in the introduction of a viscosity in order to add dissipation and is accomplished by using a relative drag between particles. Two different model viscosities have been presented and tested with the shock tube problems. Wave propagation studies reveal the model is capable of producing the correct dispersive behavior for magnetosonic and shear Alfvèn modes for all wavelengths greater than a few times the particle size or grid spacing.

The basic formulation of the particle MHD model allows for the introduction of two fluid effects in a natural way. To include some of the electron dynamics effects we use a massless electron approximation and quasi-neutrality to arrive at the Ohm's law with a Hall term. A test of this model shows the wave spectrum contains the whistler and ion cyclotron modes which are well resolved. Furthermore, we have formulated a closed set of equations with multiple ion species and the formulation is shown to provide a means for investigating the coupling between fluids through the self-consistent electric and magnetic fields.

Introduction of more physical processes may produce additional high frequency modes in the simulation, such as the whistler branch. This places con-

straints on the time step and may inhibit the study of the long time behavior or steady state of the system. Procedures for eliminating the fast mode time step constraint can be implemented in the algorithm. A semi-implicit form of the magnetic induction equation, within the framework of the Lax-Wendroff scheme, is shown to allow for unconditional stability and sufficient accuracy to advance the magnetic field with a larger time step than is given by the explicit stability criterion.

Finally, we have applied the single fluid model to an investigation of the solar wind and cometary plasma interaction. We have shown the model is capable of resolving the cometary bow shock and produces a standoff distance from the nucleus of the comet which is in agreement with a simple analytical solution. Treating the solar wind and cometary mass densities differently reveals the bow shock is able to trap and hence produce density enhancements of cometary ions in the shock region. Wave propagation studies reveal the presence of large amplitude magnetosonic and Alfvèn modes upstream of the bow shock and lower amplitude magnetoacoustic waves within the lobe region. Further investigations are currently in progress with the multiple ion fluid model, with particular attention to the wave generation and heavy ion pickup and convection. Also, the effects of Hall currents on the bow shock structure is also being studied.

Acknowledgements One of the authors (R. D. S.) would like to thank Prof. J. M. Dawson, Dr. F. Brunel and Dr. J. N. Leboeuf for helpful discussions. This work was supported by the National Science Foundation grant ATM 85–21125 and NASA grant STTP–NAGW–78 and we acknowledge the San Diego Supercomputing Center for their assistance.

References

[1] Potter D. E., *Computational Physics*, Wiley, NY, (1973).

[2] Leboeuf, J. N., Tajima, T. and Dawson, J. M., A Magnetohydrodynamic Particle Code for Fluid Simulations of Plasmas, *J. Comp. Phys.* **31**, 379–408, (1979).

[3] Birdsall, C. K. and Langdon, A. B., *Plasma Physics via Computer Simulation*, McGraw–Hill, NY, (1985).

[4] Brunel, F. et al., Magnetohydrodynamic Particle Code: Lax–Wendroff Algorithm with Finer Grid Interpolations, *J. Comp. Phys.* **43**, 268–288, (1981).

[5] Priest, E. R., *Solar System Magnetohydrodynamics*, D. Reidel Publishing Company, (1984).

[6] Braginskii, S. T., Transport Processes in a Plasma, *Rev. of Plasma Physics* **1**, 205–311, (1965).

[7] Clemmov, P. C. and Dougherty, J. P., *Electrodynamics of Particles and Plasmas*, Addison–Wesley Publishing Company, (1969).

[8] Boyd, T. J. M. and Sanderson, J. J., *Plasma Dynamics*, Barnes & Noble Inc., NY, (1969).

[9] Peyret, R. and Taylor, T. D., *Computational Methods for Fluid Flow*, Springer Series in Computational Physics, Springer, NY, (1983).

[10] Sutton, W. S. and Sherman, A., *Engineering Magnetohydrodynamics*, McGraw–Hill, NY,(1965).

[11] Tajima, T., Leboeuf, J. N. and Dawson, J. M., A Magnetohydrodynamic Particle Code with Force Free Electrons for Fluid Simulations, *J. Comp. Phys.* **38**, 237–250, (1980).

[12] Roberts, K. V. and Weiss, N. O., Convective Difference Schemes, *Math. Comp.* **20**, 272–283, (1966).

[13] Landshoff, R., A Numerical Method for Treating Fluid Flow in the Presence of Shocks, Los Alamos Scientific Report, LA–1930, (1955).

[14] Ogino, T., Walker, R. J. and Ashour–Abdalla, M., An MHD Simulation of the Interaction of the Solar Wind with the Outflowing Plasma from a Comet, *Geop. Res. Lett.* **13**, 929–932, (1986).

[15] Schmidt, H. U. and Wegmann, R., Plasma Flow and Magnetic Field in Comets, *Comets*, L. L. Wilkening ed., The University of Arizona Press, (1982).

[16] Aldrich, C. H., Particle Code Simulations with Injected Particles, *Space Sci. Rev.* **42**, 131–141, (1985).

[17] Sod, G. A., A Survey of Several Finite Difference Methods for Systems of Nonlinear Conservation Laws, *J. Comp. Phys.* **27**, 1–31, (1978).

[18] Woodward, P. and Colella, P., The Numerical Simulation of Two–Dimensional Fluid Flow with Strong Shocks, *J. Comp. Phys.* **54**, 115–173, (1984).

[19] Hughes, W. F. and Brighton, J. A., *Fluid Dynamics*, Schaums Outline Series in Engeneering, McGraw–Hill, NY, (1967).

[20] Owczarek, J. A., *Fundamentals of Gasdynamics*, International Textbook Company, (1964).

[21] Mitchner, M., Magnetohydrodynamic Flow in a Shock Tube, *Phys. Fluids* **2**, 62–71, (1959).

[22] Ip, W. H. and Axford, W. I., Theories of Physical Processes in the Cometary Coma and Ion Tail, *Comets*, L. L. Wilkening ed., The University of Arizona Press, (1982).

[23] *Nature*, special issue, **321**, No. 6067, (1986).

[24] *20th ESLAB Symposium on the Exploration of Halley's Comet*, Proceedings of the International Symposium, Heidelberg, Germany, ESA SP–250, (1986).

[25] Huebner, W. F, Giguere, P. T. and Slattery, W. L., Photochemical Processes in the Inner Coma, *Comets*, L. L. Wilkening ed., The University of Arizona Press, (1982).

[26] Johnstone, A. D., *Solar System Magnetic Fields, chap. 10*, E. R. Priest ed., D. Reidel Publishing Company, (1986).

[27] Winske, D. et al., Coupling of Newborn Ions to the Solar Wind by Electromagnetic Instabilities and their Interaction with the Bow Shock, *J. Geop. Res.* **90**, 2713–2726, (1985).

[28] Sagdeev, R. Z. et al., MHD Turbulence in the Solar Wind Comet Interaction Region, *Geop. Res. Lett.* **13**, 85–88, (1986).

[29] Omidi, N. and Winske, D., A Kinetic Study of the Solar Wind Massloading and Cometary Bow Shocks, *J. Geop. Res.*, in press, (1987).

[30] Biermann, L., Brosowski, B. and Schmidt, H. U., The Interaction of the Solar Wind with a Comet, *Solar Physics* **1**, 254–284, (1986).

[31] Brecht, S. H., Global Simulations Using MHD Codes: A Few Points to Consider Before You Try One, *Space Sci. Rev.* **42**, 169–185, (1985).

[32] Haser, L., Distribution d'intensitè dans la tête d'une comete, *Bull. Acad. Roy. Belgique (Cl. Sci.) Ser. 5* **18**, 740–750, (1957).

[33] Marochnik, L. S., Solar Wind Magnetic Field Penetration into Cometary Ionospheres, *The Moon and the Planets* **26**, 353–370, (1982).

[34] Volkov, T. F., Hydrodynamic Desription of a Collisionless Plasma, *Rev. of Plasma Physics* **4**, 1–20, (1966).

[35] Gottlieb, D. and Orszag, S. A., *Numerical Analysis of Spectral Methods: Theory and Applications*, Society for Industrial and Applied Mathematics, Philadelphia, (1977).

[36] Harned, D. S. and Kerner, W., Semi–Implicit Method for Three–Dimensional Magnetohydrodynamic Simulation, *J. Comp. Phys.* **60**, 62, (1985).